CYLINDRICALLY AND SPHERICALLY CONSTRAINED FAMILIES OF NON-KEPLERIAN ORBITS

Jeannette Heiligers,[*] and Colin R. McInnes[†]

This paper introduces new families of Sun-centered non-Keplerian orbits (NKOs) that are constrained to a three-dimensional surface such as a cylinder or sphere. As such, they are an extension to the well-known families of two-dimensional NKOs. For both the cylindrical and spherical types of orbits, the equations of motion are derived in an appropriate reference frame, constraints are introduced to confine the orbit to a cylindrical or spherical surface and further constraints allow the definition of the set of feasible orbits. Additionally, the phase spaces of the orbits are explored and a numerical analysis is developed to find periodic orbits within the set of feasible orbits. The richness of the problem is further enhanced by considering both an inverse square acceleration law (mimicking solar electric propulsion) and a solar sail acceleration law to keep the spacecraft on the cylindrical or spherical surface. These new families of NKOs generate a wealth of new orbits with a range of interesting applications ranging from solar physics to astronomy and planetary observation.

INTRODUCTION

By exploiting a continuous propulsive force, non-Keplerian orbits (NKOs) strongly perturb the two- or three body problem, thereby creating a wealth of new orbits for the spacecraft motion about the central body. A particular subset of non-Keplerian orbits in the two-body problem are the so-called displaced NKOs,[1] where the continuous acceleration is applied perpendicular to – or in - the orbit plane to displace the orbit away from the natural Keplerian orbit. The dynamics of such two-body displaced NKOs have been investigated before[2] by considering the spacecraft's equations of motion in a rotating frame of reference to make the problem autonomous. Equilibrium solutions of these equations of motion will then provide the sought for displaced NKOs and a transformation to an inertial frame will subsequently show that the spacecraft executes a circular orbit displaced away from the natural Keplerian orbit. The applications of such displaced NKOs are abundant and their potential has been shown in a range of studies, both Sun-centered and planet-centered. In the Sun-centered case, applications include solar physics and one year orbits synchronous with the Earth for space weather monitoring,[3] while the planet-centered case include applications such as displaced geostationary orbits,[4, 5] hovering above Saturn's rings for high-resolution imaging[6] and NKOs displaced behind the Earth to observe the structure of the geomagnetic tail.[7]

In order to increase the wealth of NKOs and their applications even further, this paper will extend the families of displaced NKOs, which are two-dimensional (2D), with families of three-dimensional (3D) NKOs, particularly those that are confined to a cylindrical or spherical surface. Feasible orbits will be

---

[*] Research Associate, Advanced Space Concepts Laboratory, Department of Mechanical and Aerospace Engineering, University of Strathclyde, 75 Montrose Street, Glasgow, G1 1XJ, U.K., jeannette.heiligers@strath.ac.uk.
[†] Director, Advanced Space Concepts Laboratory, Department of Mechanical and Aerospace Engineering, University of Strathclyde, 75 Montrose Street, Glasgow, G1 1XJ, U.K., colin.mcinnes@strath.ac.uk.

found by constraining the dynamics of the spacecraft in a cylindrical or spherical coordinate system and imposing further constraints on the orbit angular velocity and acceleration magnitude. Furthermore, the system's phase space will be explored to identify new families of NKOs and Poincaré maps will be used to demonstrate the periodicity of the orbit. Finally, true periodic orbits will be found through a newly developed numerical analysis.

As this paper will demonstrate, a range of 3D NKOs is created, including orbits that cover only a narrow band on the cylindrical or spherical surface for dedicated observations and those that cover nearly the entire surface for a full mapping of the central body. While orbits confined to a cylindrical surface are extremely useful for hovering above a target such as the previously mentioned rings of Saturn, orbits that lie on a spherical surface remain at a constant distance to the central body, which is ideal for precise remote sensing of the central body, e.g. for solar physics and solar polar investigations. Other identified applications include interplanetary communication and astronomical observations.

Despite the interesting applications for the planet-centered case, this paper will focus on the Sun-centered case and leave the planet-centered case for future work. Furthermore, in order to generate the 3D NKOs, two types of propulsion will be considered: one for which the acceleration is proportional to the Sun-spacecraft distance squared (mimicking solar electric propulsion (SEP)), thereby extending previous work on cylindrically and spherically constrained non-Keplerian orbits,[8] and one which follows an ideal solar sail acceleration law. While SEP is a well-established propulsion technology with flight heritage on missions such as JAXA's Hayabusa (2003),[9] NASA's Dawn mission (2007)[10] and ESA's GOCE mission (2009),[11] solar sail technology is usually considered more far-term. However, with recent advances through JAXA's IKAROS mission (2010)[12] and NASA's NanoSail-D2 mission (2010)[13] and new solar sail initiatives scheduled for the future, including NASA's Sunjammer mission,[14] solar sail technology is rapidly developing, bringing the solar sail 3D NKOs more and more into reach.

To introduce these novel 3D cylindrical and spherical NKOs, the structure of the paper will be as follows. First, the cylindrical case will be presented: the equations of motion, control law and constraints required to remain on a cylindrical surface will be obtained. Depending on a sign choice in the differential equation for the out-of-plane motion, two families of orbits can be distinguished, which both will be considered as well as the two different types of propulsive accelerations. For each case, the set of feasible orbits will be derived, example orbits will be shown and periodic orbits will be sought for. A very similar analysis will be performed for the spherical case and the paper ends with the conclusions.

CYLINDRICALLY CONSTRAINED NKOS

Cylindrically constrained orbits can be found by considering the two-body equations of motion in a cylindrical coordinate system (ρ, θ, z) as shown in Figure 1a. By assuming a central gravitational force field and an acceleration in the (ρ, z)-plane only, the equations of motion can be written as:

$$\ddot{\rho} - \rho\dot{\theta}^2 = -\frac{\mu}{r^3}\rho + a\cos(\alpha + \gamma)$$
$$\rho^2\ddot{\theta} + 2\rho\dot{\rho}\dot{\theta} = 0 \tag{1}$$
$$\ddot{z} = -\frac{\mu}{r^3}z + a\sin(\alpha + \gamma)$$

with α the acceleration angle with respect to the radial direction, also known as the cone angle, and γ the elevation angle of the spacecraft.

To remain on a cylindrical surface, the following constraint on the projected radius ρ is introduced: $\rho = \text{constant} \rightarrow \dot{\rho} = \ddot{\rho} = 0$. Furthermore, introducing the parameter $\bar{\omega} = \sqrt{\mu/\rho^3}$, which equals the angular velocity of a Keplerian orbit with radius ρ, the equations of motion reduce to:

$$\cos(\alpha+\gamma) = \frac{\rho\bar{\omega}^2}{a}\left(\left(1+\left(\frac{z}{\rho}\right)^2\right)^{-\frac{3}{2}} - \left(\frac{\omega}{\bar{\omega}}\right)^2\right)$$

$$\ddot{\theta} = 0 \rightarrow \dot{\theta} = \text{constant} = \omega \tag{2}$$

$$\ddot{z} = -z\bar{\omega}^2\left(1+\left(\frac{z}{\rho}\right)^2\right)^{-\frac{3}{2}} \pm a\sqrt{1-\cos^2(\alpha+\gamma)}$$

The first equation in Eq. (2) provides the control law required to stay on a cylindrical surface, the second equation shows that the in-plane angular velocity is constant, which will be denoted by ω, and the third equation describes the spacecraft's motion in the out-of-plane direction. With initial conditions $z(0)=z_0$, $\dot{z}(0)=0$, this out-of-plane motion resembles a highly non-linear oscillator. Note that the plus-sign in the third equation has been replaced by a $\pm$-sign as this generates two distinct families of cylindrical orbits. As will become clear in the next few sections, the minus-sign (which mirrors the acceleration in the (x,y)-plane) results in cylindrical orbits that oscillate around the (x,y)-plane, i.e. $-z_0 \le z(t) \le z_0$, while the plus-sign offers the possibility for the orbit to oscillate around a plane parallel to – and above - the (x,y)-plane, thereby covering a narrower band on the cylindrical surface. The family of orbits associated with the minus-sign will hereafter be referred to as *oscillating orbits*, while the family of orbits associated with the plus-sign will be referred to as *banded orbits*. They will first be considered for an inverse square acceleration law, followed by a similar analysis for a solar sail acceleration law.
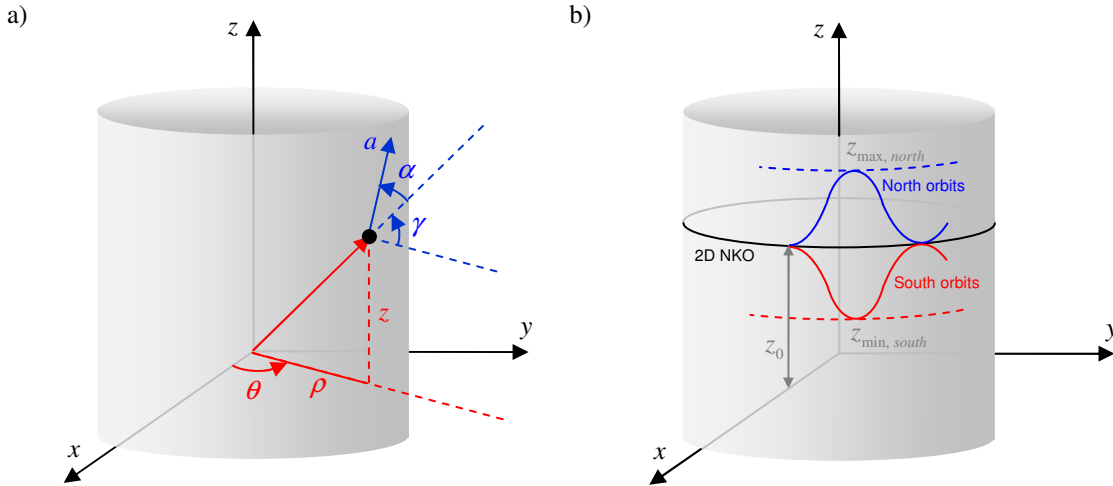
Figure 1. a) Definition of cylindrical reference frame. b) Definition of north and south banded orbits.

Inverse square acceleration law

The inverse-square acceleration law that is adopted to mimic an SEP acceleration is given by:

$$a = \beta_{SEP}\frac{\mu}{r^2} = \beta_{SEP}\bar{\omega}^2\rho\left(1+\left(\frac{z}{\rho}\right)^2\right)^{-1} \tag{3}$$

with β_{SEP} a scaling factor. Indeed, for the Sun-centered case, it can be roughly assumed that the SEP acceleration scales with the distance to the Sun, r, squared (for now, assuming a constant spacecraft mass).

3

Using the acceleration in Eq. (3), feasible orbits are found only if $-1 \leq \cos(\alpha + \gamma) \leq 1$. From the first equation in Eq. (2), the following constraints on the in-plane angular velocity, ω, and the scaling factor, β_{SEP}, can then be derived:

$$\omega \leq \bar{\omega} \sqrt{\beta \left(1 + \left(\frac{z}{\rho}\right)^2\right)^{-1} + \left(1 + \left(\frac{z}{\rho}\right)^2\right)^{-\frac{3}{2}}}, \quad \beta_{SEP} \geq \left(1 + \left(\frac{z}{\rho}\right)^2\right) \left(\left(1 + \left(\frac{z}{\rho}\right)^2\right)^{-\frac{3}{2}} - \left(\frac{\omega}{\bar{\omega}}\right)^2\right) \tag{4}$$

Since $\rho, \omega, \bar{\omega}$ and β_{SEP} are constant, both constraints vary only with the out-of-plane displacement, z. However, this implies that the values for ω and β_{SEP} should be chosen carefully to make sure that the constraints are satisfied along the entire orbit. Since the minimum value for the right-hand sight of the left equation in Eq. (4) occurs at the maximum value for z, z_{max}, the constraint on ω should be evaluated at z_{max}. A similar reasoning can be adopted for the constraint on the scaling factor, β_{SEP}. Only now, the maximum value for the right-hand side of the right equation in Eq. (4) occurs at the minimum *absolute* value for z, z_{min}. The constraint on β_{SEP} should therefore be evaluated at z_{min}. The actual values for z_{min} and z_{max} depend on the family of orbits considered as will become clear in the following.

Family of oscillating orbits

As indicated above, by applying the minus sign in the third equation of Eq. (2), orbits originate that oscillate around the (x, y)-plane such that $-z_0 \leq z(t) \leq z_0$. Then, it is immediately clear that $z_{min} = 0$ and $z_{max} = z_0$. The constraints in Eq. (4) therefore reduce to:

$$\omega \leq \bar{\omega} \sqrt{\beta \left(1 + \left(\frac{z_0}{\rho}\right)^2\right)^{-1} + \left(1 + \left(\frac{z_0}{\rho}\right)^2\right)^{-\frac{3}{2}}}, \quad \beta_{SEP} \geq 1 - \left(\frac{\omega}{\bar{\omega}}\right)^2 \tag{5}$$

These constraints can be evaluated analytically, resulting in the region of feasible oscillating cylindrical orbits with an inverse square acceleration law as shown in Figure 2 for $\rho = 0.9$ and $z_0 = 0.5$, a case which will be considered throughout this paper. Note that the results in the figure and any subsequent figures are made dimensionless by setting $\rho = 1$ and $\bar{\omega} = 1$. The non-dimensional time of one full revolution therefore equals 2π.
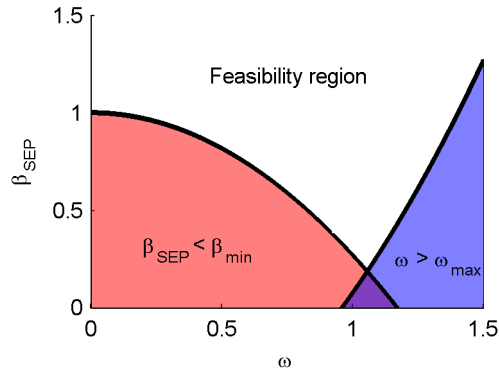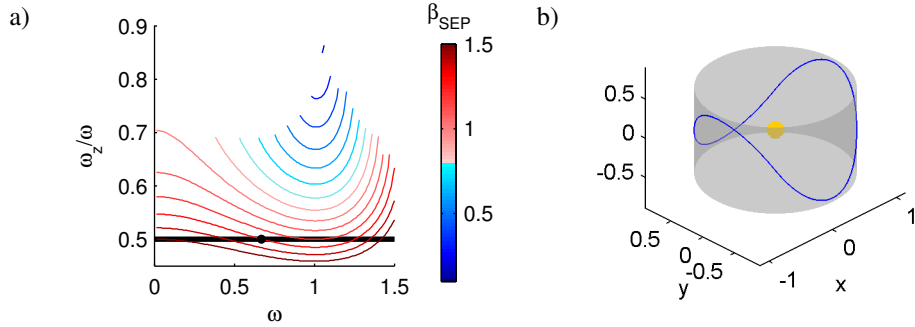

Figure 2 Feasibility region for oscillating, cylindrical NKOs with inverse-square acceleration law for $\rho = 0.9$ and $z_0 = 0.5$.

A first impression of the types of oscillating, cylindrically constrained NKOs that are feasible is provided in Figure 3 for two particular values of the scaling factor. The figures clearly show that these types of orbits oscillate around the (x, y)-plane and move between $z = z_0$ and $z = -z_0$. The figure also includes the Poincaré maps of the orbits, showing the system's phase space after each full revolution (with a maximum of 20 revolutions), which indicate that the orbits are quasi-periodic, especially the orbit in Figure 3b. True periodic orbits are therefore sought for using the numerical analysis described below.
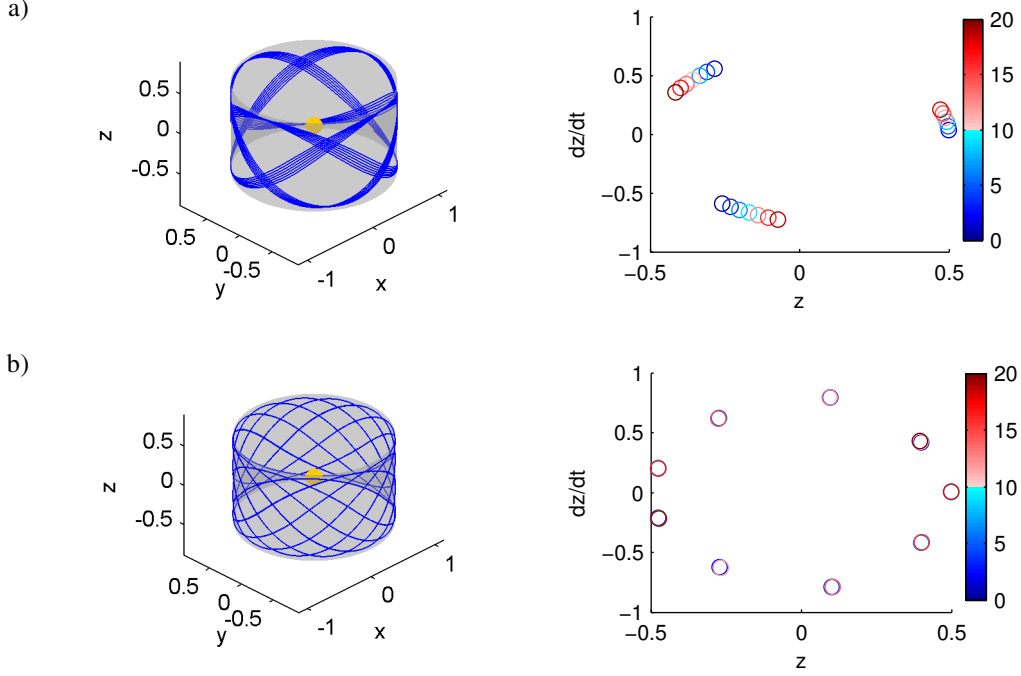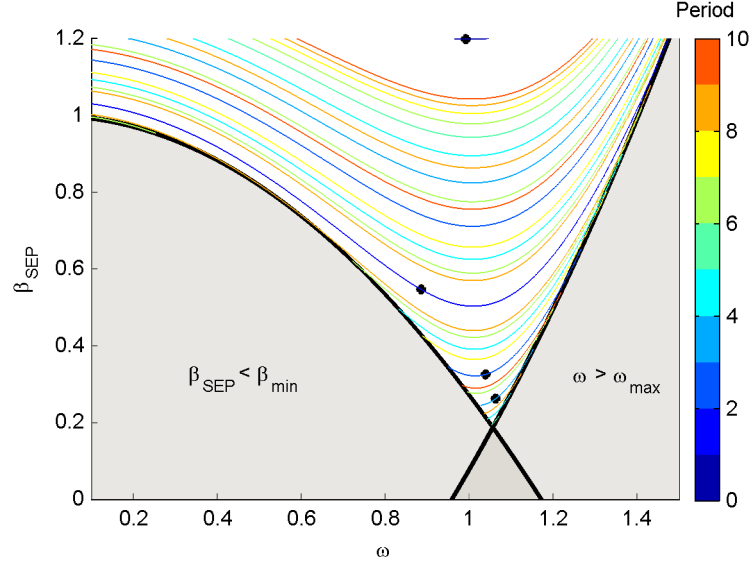

Figure 3 Orbital plots and Poincaré maps for oscillating, cylindrical NKOs with inverse-square acceleration law for $\rho = 0.9$, $z_0 = 0.5$ and $\omega = 1$. a) $\beta_{SEP} = 0.32$. b) $\beta_{SEP} = 0.44$.
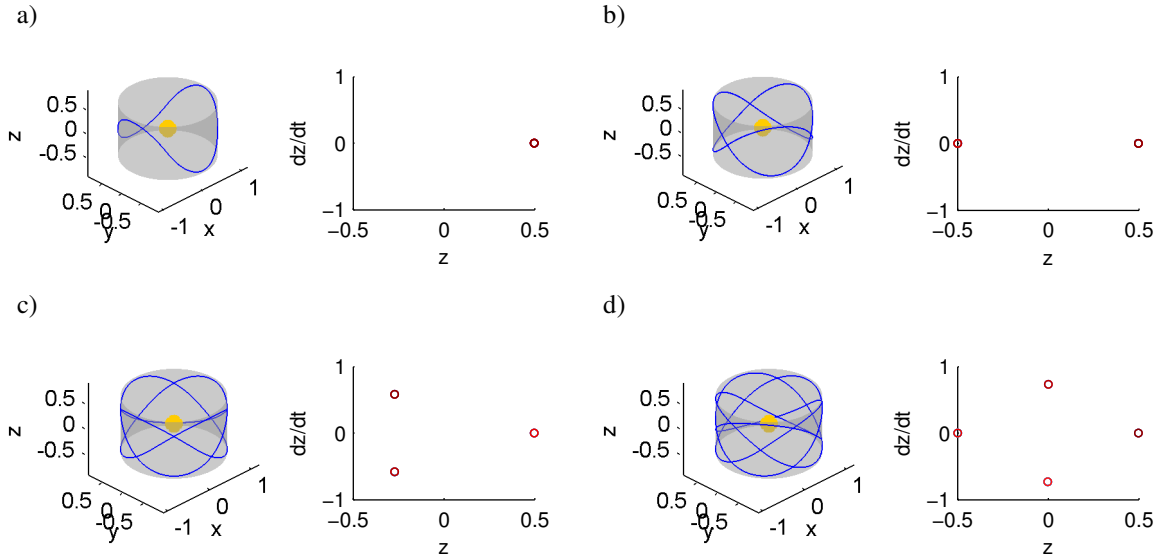

Figure 4 Oscillating, cylindrical NKOs with inverse-square acceleration law for $\rho = 0.9$ and $z_0 = 0.5$. a) Ratio of out-of-plane and in-plane angular velocities. b) Example periodic orbit (see black dot in plot a)) with $\omega = 0.6675$ and $\beta_{SEP} = 1.3$.

In order to obtain true periodic orbits, the initial conditions are integrated forward until the orbit crosses the (x, y)-plane, which occurs at time $t = t_{z=0}$. Due to symmetry, a full period of the orbit, P, equals $P = 4t_{z=0}$. Using the dimensionless time as introduced above Figure 2, this period can be expressed as a

fraction of a full revolution as $4t_{z=0}/2\pi$, which also equals the ratio of the out-of-plane angular velocity, ω_z, and the in-plane angular velocity, ω: $\omega_z/\omega = 4t_{z=0}/2\pi$. If this fraction equals an irreducible fraction (e.g. $1/2$, $2/3$, $4/5$, etc.) the orbit is periodic, where the period is given by the nominator of the irreducible fraction. An example is given in Figure 4, which provides the ratio of out-of-plane and in-plane angular velocities for $\rho = 0.9$ and $z_0 = 0.5$ and for a range of in-plane angular velocities and scaling factors. The black line in the figure represents one particular ratio, $\omega_z/\omega = 1/2$. Each intersection of the curved lines and this black line is a true periodic orbit with a period of one revolution. An example of such an orbit is given in Figure 4b, which corresponds to the black dot in Figure 4a.

Figure 5 Periodic orbits for oscillating, cylindrical NKOs with inverse-square acceleration law for $\rho = 0.9$ and $z_0 = 0.5$. The black dots correspond to the orbits in Figure 6.

a)   b)

c)   d)

Figure 6 Orbits (see black dots in Figure 5) and Poincaré maps for oscillating, cylindrical NKOs with inverse-square acceleration law for $\rho = 0.9$ and $z_0 = 0.5$. a) $\omega = 0.991$, $\beta_{SEP} = 1.198$. b) $\omega = 0.885$, $\beta_{SEP} = 0.547$. c) $\omega = 1.038$, $\beta_{SEP} = 0.326$. d) $\omega = 1.062$, $\beta_{SEP} = 0.263$.

Through a fine grid search over values for ω and β_{SEP} and by using an interpolation scheme to accurately determine the intersections, the periodic orbits in Figure 5 are obtained. A maximum period of 10 revolutions is considered, implying that all irreducible fractions with a maximum nominator of 10 are accounted for. The figure furthermore shows that lines of equal periods exist in the feasibility region of oscillating, cylindrical orbits. Finally, some examples of true periodic orbits are shown in Figure 6, which correspond to the black dots in Figure 5.

Family of banded orbits

When considering the plus-sign in the third equation of Eq. (2), an additional family of cylindrical NKOs orbits can be found, so-called banded cylindrical orbits. This family will include the well-known 2D displaced NKOs that were discussed in the introduction of this paper, since these 2D orbits can be considered to lie on a cylindrical surface. Furthermore, since these 2D NKOs maintain a constant out-of-plane displacement, $z(t) = z_0$, the required scaling factor to achieve these 2D NKOs, $\beta_{SEP, 2D}$, can be found by setting $\ddot{z} = 0$ in Eq. (2):

$$\beta_{SEP, 2D} = \sqrt{\left[1+\left(\frac{z}{\rho}\right)^2\right]^{-1}\left(\left(\frac{z}{\rho}\right)^2 + \left[\left(\frac{\omega}{\bar{\omega}}\right)^2\left(1+\left(\frac{z}{\rho}\right)^2\right)^{\frac{3}{2}} - 1\right]\right)^2}$$

(6)

By substituting Eq. (6) into the constraints defined in Eq. (4), it can be shown that these 2D NKOs are feasible for all ω.

By increasing or decreasing β_{SEP} with respect to $\beta_{SEP, 2D}$, while still satisfying the control law in the first equation of Eq. (2), the family of banded cylindrical NKOs can be found. As will become clear later, by *increasing* β_{SEP} with respect to $\beta_{SEP, 2D}$, orbits that lie entirely *above* the 2D NKO from which they bifurcate are created. This sub-family will be referred to as 'north orbits', see Figure 1b. Contrary, by *decreasing* β_{SEP} with respect to $\beta_{SEP, 2D}$, a sub-family of orbits that lie entirely *below* the 2D NKO are created, which will be referred to as 'south orbits', see again Figure 1b. This distinction has implications on the evaluation of the constraints in Eq. (4), as will be explained hereafter.

As stated before, to evaluate the maximum allowable value for ω, the value for z_{max} is required, which is known for south orbits ($z_{max} = z_0$) but is unknown for north orbits, since it is unknown a priori how much the north orbit will deviation from the 2D NKO, see also Figure 1b. For north orbits, the constraint on ω can therefore only be determined numerically through an integration of the orbit and by determining whether or not the maximum allowable in-plane angular velocity is exceeded. Instead, for south orbits (indicated by the subscript 'south'), the constraint can be evaluated analytically as:

$$\omega_{south} \leq \bar{\omega}\sqrt{\beta\left(1+\left(\frac{z_0}{\rho}\right)^2\right)^{-1} + \left(1+\left(\frac{z_0}{\rho}\right)^2\right)^{-\frac{3}{2}}}$$

(7)

Contrary, to evaluate the minimum required value for β_{SEP}, the value of z_{min} is required, which is known for north orbits ($z_{min} = z_0$), but can again only be obtained through an integration of the orbit for south orbits. The analytical constraint on β_{SEP} for north orbits (indicated by the subscript 'north') is thus:

$$\beta_{SEP, north} \geq \left(1+\left(\frac{z_0}{\rho}\right)^2\right)\left(\left(1+\left(\frac{z_0}{\rho}\right)^2\right)^{-\frac{3}{2}} - \left(\frac{\omega}{\bar{\omega}}\right)^2\right)$$

(8)

7

The result of a combined analytical and numerical computation of the feasibility region for banded, cylindrical NKOs with an inverse square acceleration law and for the case $\rho = 0.9$ and $z_0 = 0.5$ is given in Figure 7, where the red line represents the value for $\beta_{SEP,2D}$. All feasible orbits above this red line (i.e. $\beta_{SEP} > \beta_{SEP,2D}$) are north orbits, those below the red line are south orbits (i.e. $\beta_{SEP} < \beta_{SEP,2D}$). Furthermore, the figure includes the constraints in Eqs. (7) and (8) through the use of a thick blue and yellow line, respectively. Note that the yellow line, which gives the minimum value for β_{SEP} for north orbits lies within the infeasible region for south orbits and below the red line for $\beta_{SEP,2D}$, again indicating that 2D NKOs are feasible for all ω.
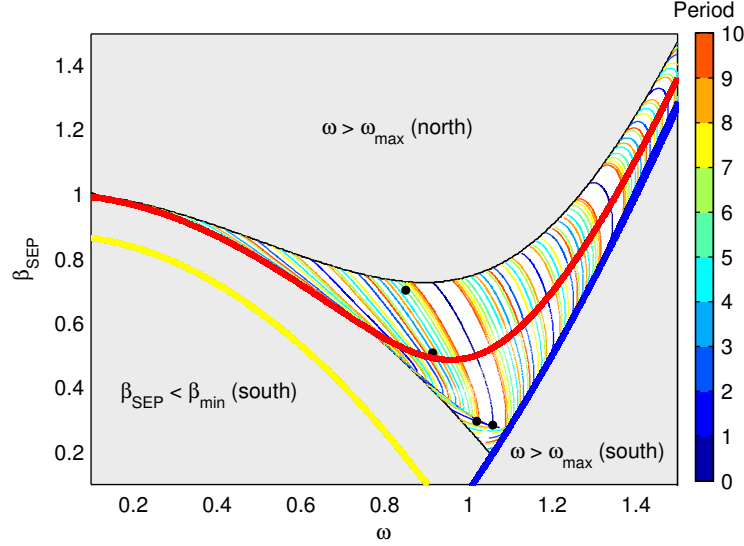

Figure 7 Feasibility region including periodic orbits for banded, cylindrical NKOs with inverse-square acceleration law for $\rho = 0.9$ and $z_0 = 0.5$. The thick blue line equals Eq. (7), the thick yellow line equals Eq. (8). The black dots correspond to the orbits in Figure 9.

The feasibility region in Figure 7 can also be represented through the system's phase space, which gives an insight in the actual shape of the cylindrical orbits, see Figure 8a. The phase space gives the out-of-plane motion, z, and out-of plane velocity, $\dot{z}$, for each combination of ω (on z-axis) and β_{SEP} (through color). However, rather than using the absolute value for β_{SEP}, Figure 8a expresses the scaling factor as a percentage deviation from $\beta_{SEP,2D}$, $\Delta\beta_{SEP}$. Furthermore, black dots are used on a gray transparent surface to represent the 2D NKOs. Therefore, the phases to the right of this surface are north orbits, for which $\Delta\beta_{SEP} > 0$ (red color), while phase spaces to the left of this surface are south orbits for which $\Delta\beta_{SEP} < 0$ (blue color). Some examples of both north and south orbits are provided in Figure 8b, where the black line indicates the 2D NKO from which the cylindrical orbit bifurcates.

From the phase space in Figure 8a and the example orbits in Figure 8b it becomes clear that north and south orbits move in a confined band above or below the 2D displaced NKO, respectively. Furthermore, for some cases, the value for β_{SEP} can be decreased to such extent that the phase space crosses the (x, y)-plane after which it immediately transforms into the phase space of an oscillating orbit, i.e. $-z_0 \leq z \leq z_0$. This is, for example, the case for $\omega = 1.0$ and $\Delta\beta_{SEP} = -40\%$ (see also plot 1 in Figure 8b). The phase space finally shows that, the larger $\Delta\beta_{SEP}$, the farther the orbit deviates from the 2D NKO, i.e. the wider the band covered on the cylindrical surface. Additionally, the larger value for ω, the narrower the band covered for a particular value for $\Delta\beta_{SEP}$. This has an interesting application as will be explained in the next paragraph.
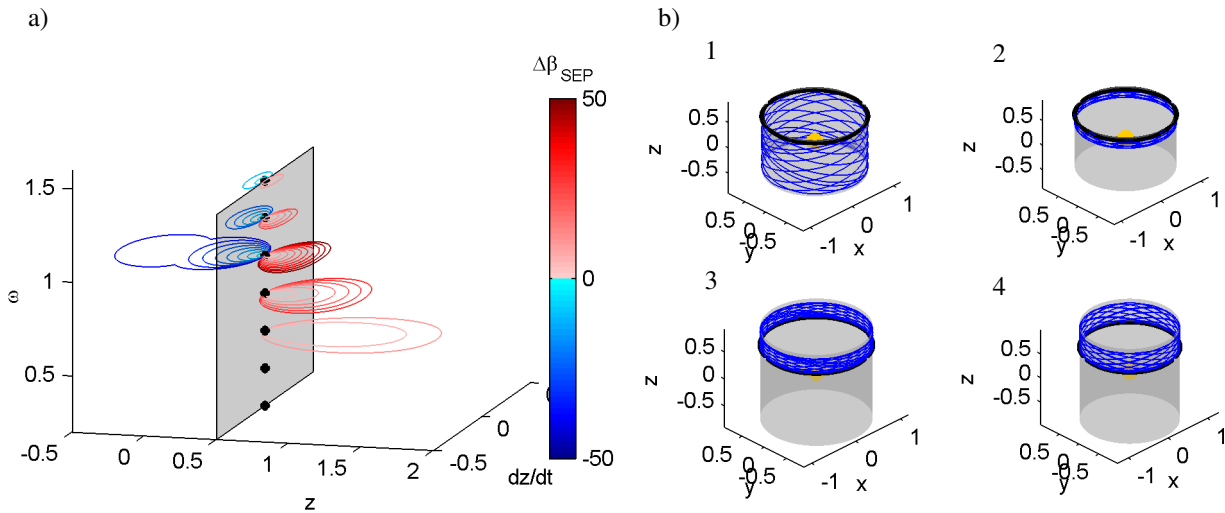
Figure 8 Banded, cylindrical NKOs with inverse-square acceleration law for $\rho = 0.9$ and $z_0 = 0.5$. a) Phase spaces. Colors indicate percentage deviation from $\beta_{SEP,2D}$ with a step size of 5%. b) Example orbits for $\omega = 1.0$ and different values for $\Delta\beta_{SEP}$: 1) -40%, 2) -15%, 3) 30%, 4) 50%.

An interesting application of the cylindrical orbits follows from the phase space in Figure 8 and, for example, from the orbit in plot 2 of Figure 8b: by reducing β_{SEP} below $\beta_{SEP,2D}$, less demanding propulsion technology than for the 2D NKO is required, while in some cases the cylindrical orbit stays very close to the 2D NKO. For example, the orbit in plot 2 of Figure 8b allows for a 15 percent reduction in the required scaling factor while not deviating much from the original 2D NKO. This advantage occurs mainly for large values for the in-plane angular velocity, see Figure 8, where the blue lines remain close to the 2D NKO. In case such a deviation is allowed, the cylindrical NKO could introduce significant savings over the 2D case for a range of applications, e.g. the previously mentioned application of Saturn's rings observations if a planet-centered case is considered.
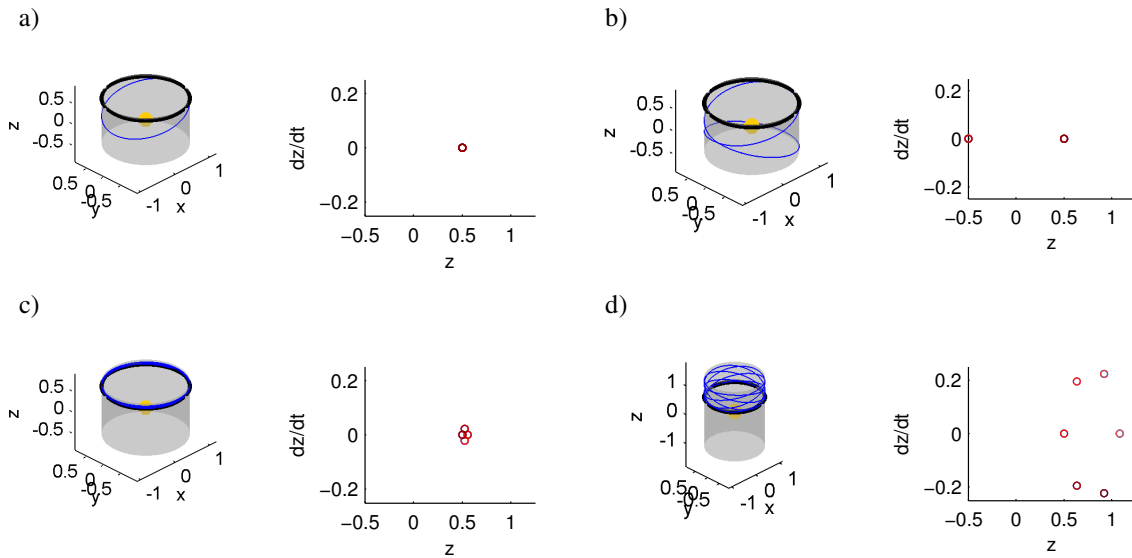
Figure 9 Orbits (see black dots in Figure 7) and Poincaré maps for banded, cylindrical NKOs with inverse-square acceleration law for $\rho = 0.9$ and $z_0 = 0.5$. a) $\omega = 1.058$, $\beta_{SEP} = 0.283$. a) $\omega = 1.020$, $\beta_{SEP} = 0.296$. c) $\omega = 0.915$, $\beta_{SEP} = 0.508$. d) $\omega = 0.850$, $\beta_{SEP} = 0.703$.

Some of the orbits in Figure 8b, e.g. plot 4, again suggest the existence of periodic orbits. To find true periodic orbits for the banded cylindrical case, an approach very similar to the one described for the oscillating cylindrical orbits on page 5 is used. Only now, since the orbit does not cross the (x, y)-plane in all cases, the integration is not truncated upon crossing the (x, y)-plane, but after one full oscillating motion. The ratio of out-of-plane and in-plane angular velocities then becomes: $\omega_z / \omega = t_P / 2\pi$, which is used to establish the periodicity of the orbits. The result can be found in Figure 7, with some typical banded cylindrical orbits in Figure 9.

Solar sail acceleration law

The second type of acceleration that will be considered for the cylindrical NKOs is an ideal solar sail acceleration. From Reference 15 and following the definitions in Figure 1, the solar sail acceleration is given by:

$$a = \beta_s \frac{\mu}{r^2} \cos^2 \alpha = \beta_s \bar{\omega}^2 \rho \left(1 + \left(\frac{z}{\rho}\right)^2\right)^{-1} \cos^2 \alpha \qquad (9)$$

with β_s the sail lightness number, which is the ratio of the solar radiation pressure acceleration and the solar gravitational acceleration, or can equivalently be described as a function of the ratio of the spacecraft mass and the solar sail area. Substituting this acceleration into the first equation of Eq. (2), gives the required control law in implicit form:

$$\cos(\alpha + \gamma)\cos^2 \alpha = \cos\left(\alpha + \tan^{-1}\left(\frac{z}{\rho}\right)\right)\cos^2 \alpha = \frac{1}{\beta_s}\left(1 + \left(\frac{z}{\rho}\right)^2\right)\left(\left(1 + \left(\frac{z}{\rho}\right)^2\right)^{-\frac{3}{2}} - \left(\frac{\omega}{\bar{\omega}}\right)^2\right) \qquad (10)$$

To solve Eq. (10) for $\cos \alpha$, the roots of the following sixth order polynomial need to be found:

$$x^6 + \left(a^2 - 1\right)x^4 - 2abx^3 + b^2 = 0 \qquad (11)$$

with $x = \cos \alpha$, $a = \cos \gamma$ and $b = (1/\beta_s)\left(1 + (z/\rho)^2\right)\left(\left(1 + (z/\rho)^2\right)^{-\frac{3}{2}} - (\omega/\bar{\omega})^2\right)$. From Descartes rule of signs,[16] it follows that this polynomial has a maximum of 2 positive and 2 negative real roots. The negative roots can be discarded, since for a solar sail acceleration law, the constraint on $\cos \alpha$ is tightened (i.e. $\cos \alpha \geq 0$) due to the inability of a solar sail to generate an acceleration component in the direction of the Sun. Only a maximum of two positive real roots remain. However, since the original equation in Eq. (10) only has 3 real roots, in general only one of the two positive real roots remain.

Family of banded orbits

For brevity, only the family of banded cylindrical orbits will be considered for the solar sail acceleration law. Especially, since by significantly decreasing β_s with respect to the value for $\beta_{s,2D}$, oscillating orbits can also be obtained within the family of banded orbits, as already seen in Figure 8 for the inverse square acceleration law. This means that only the plus-sign in the third equation of Eq. (2) will be considered as well as $\alpha \geq 0$, i.e. the cone angle is always away from the radial direction in counterclockwise direction. The condition $\alpha \geq 0$ follows automatically from evaluating $\cos^{-1} x$ since the information on the sign of α is not contained in x. Evaluating $\cos^{-1} x$ will therefore by default return positive values for α.

In addition to the constraint on the cone angle, the constraints $-1 \le \cos(\alpha + \gamma) \le 1$ also need to be taken into account. Due to the lack in an explicit expression for $\cos \alpha$ (and thus also for $\cos(\alpha + \gamma)$), these constraints cannot be expressed as an analytical formulation for the maximum allowed in-plane angular velocity and the minimum required sail lightness number. These constraints can therefore only be enforced within the integration of motion, leading to a truncation of the integration when either of the constraints is violated. This results in the region of feasibility for banded, solar sail cylindrical orbits as shown in Figure 10, again for the test case $\rho = 0.9$ and $z_0 = 0.5$. The red line once again represents the lightness number, β_s, required to maintain the 2D NKO, which is given through:[15]

$$\beta_{s,2D} = \left(1 + \left(\frac{z}{\rho}\right)^2\right)^{\frac{1}{2}} \left(\left(\frac{z}{\rho}\right)^2 + \left(1 - \left(\frac{\omega}{\bar{\omega}_r}\right)^2\right)^2\right)^{\frac{3}{2}} \left(\left(\frac{z}{\rho}\right)^2 + \left(1 - \left(\frac{\omega}{\bar{\omega}_r}\right)^2\right)\right)^{-2} \tag{12}$$

with $\bar{\omega}_r = \sqrt{\mu/r^3}$ and $r = \sqrt{\rho^2 + z^2}$. Note that the sharp edge on the right side of the feasibility region is very close to the maximum value for the in-plane angular velocity for which the 2D NKO still exists, $\omega_{2D,max}$. This limit is given by:[15]

$$\omega_{2D,max} \le \sqrt{\frac{\mu}{r\rho^2}} \tag{13}$$

Close to this limit, the required value for $\beta_{s,2D}$ increases greatly as Figure 10 shows, and only lightness numbers close to these large values for $\beta_{s,2D}$ provide feasible cylindrical orbits, which far exceed the interval considered for β_s in Figure 10.
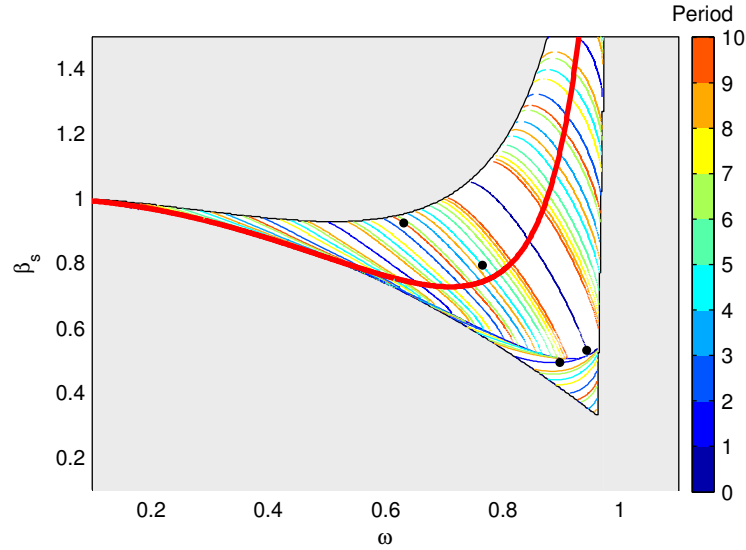
Figure 10 Feasibility region including periodic orbits for banded, cylindrical NKOs with solar sail acceleration law for $\rho = 0.9$ and $z_0 = 0.5$. The black dots correspond to the orbits in Figure 11.

Finally, the same analysis as for the banded cylindrical orbits with an inverse square law is applied to find true periodic orbits for the solar sail case. The result is included in Figure 10 with some typical solar sail periodic orbits in Figure 11.
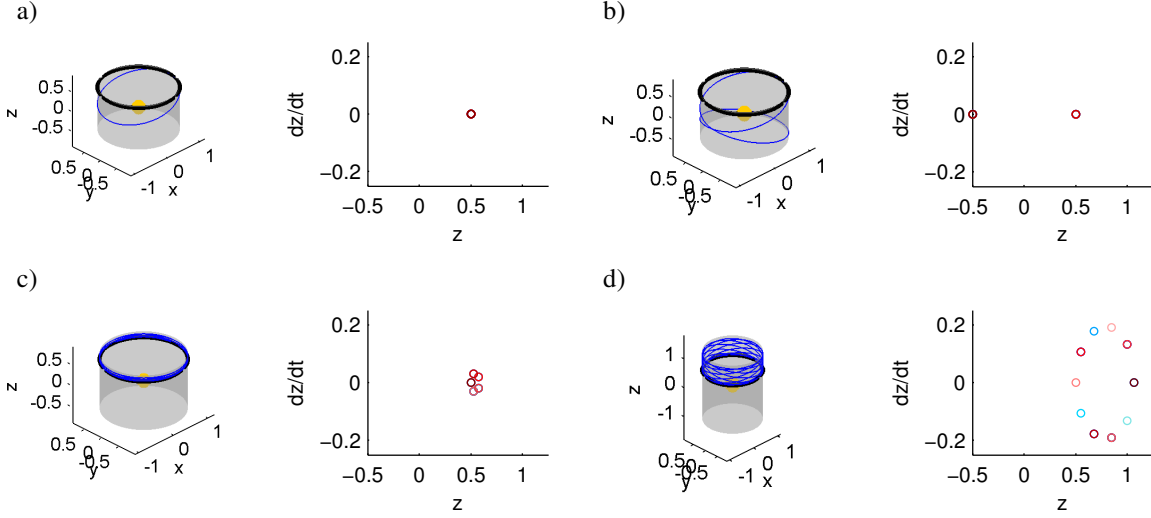
Figure 11 Orbits (see black dots in Figure 10) and Poincaré maps for banded, cylindrical NKOs with solar sail acceleration law for $\rho = 0.9$ and $z_0 = 0.5$. a) $\omega = 0.943$, $\beta_s = 0.530$. b) $\omega = 0.897$, $\beta_s = 0.492$. c) $\omega = 0.765$, $\beta_s = 0.793$. d) $\omega = 0.631$, $\beta_s = 0.924$.

SPHERICALLY CONSTRAINED NKOS

The approach to find spherically constrained NKOs is very similar to the one taken to find cylindrically constrained orbits. However, now the equations of motion are considered in a spherical coordinate system (r, θ, ϕ) as shown in Figure 12. Again, assuming a central gravitational force field and an acceleration in the (r, ϕ)-plane only, the equations of motion can be written as:

$$\ddot{r} - r\dot{\theta}^2 \cos^2 \phi - r\dot{\phi}^2 = -\frac{\mu}{r^2} + a\cos\alpha$$
$$r\cos\phi\ddot{\theta} + 2\dot{r}\dot{\theta}\cos\phi - 2r\dot{\theta}\dot{\phi}\sin\phi = 0 \tag{14}$$
$$r\ddot{\phi} + 2\dot{r}\dot{\phi} + r\dot{\theta}^2 \sin\phi\cos\phi = \pm a\sin\alpha$$

To remain on a spherical surface, a constraint on the radius r is introduced, $r = \text{constant} \rightarrow \dot{r} = \ddot{r} = 0$, and the parameter $\bar{\omega}$ that was used for the cylindrical case is changed into $\bar{\omega}_r = \sqrt{\mu/r^3}$, which now equals the angular velocity of a Keplerian orbit with radius r. The equations of motion then reduce to:

$$\cos\alpha = \frac{r}{a}\left(\bar{\omega}_r^2 - \dot{\theta}^2 \cos^2 \phi - \dot{\phi}^2\right)$$
$$\ddot{\theta} = 2\dot{\theta}\dot{\phi}\tan\phi \tag{15}$$
$$\ddot{\phi} = -\dot{\theta}^2 \sin\phi\cos\phi \pm \frac{a}{r}\sin\alpha$$

The first equation once again provides the required control law. The second equation shows that, contrary to the cylindrical case, the in-plane angular velocity, $\dot{\theta}$, is not constant. And finally, with initial conditions $\phi(0) = \phi_0$, $\dot{\phi}(0) = 0$, the third equation again resembles a highly non-linear oscillator and a ±-minus sign is included in front of the acceleration term to generate the two families of orbits discussed for the cylindrical case: oscillating orbits (for the minus-sign) and banded orbits (for the plus-sign).
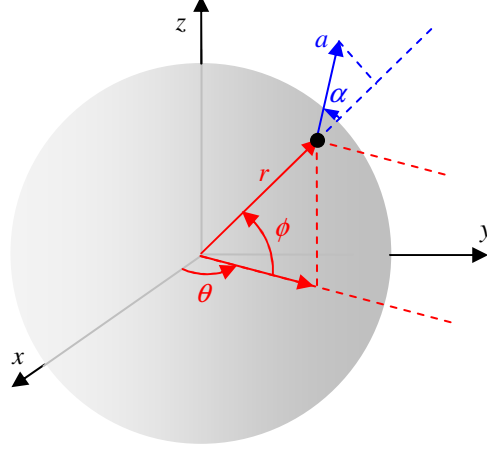
Figure 12 Definition of cylindrical reference frame.

Inverse square acceleration law

Using the new definition for $\bar{\omega}_r$, the inverse-square acceleration law can now be written as:

$$a = \beta_{SEP} \frac{\mu}{r^2} = \beta_{SEP} \bar{\omega}_r^2 r \tag{16}$$

which is constant on the spherical surface and reduces the equations of motion to:

$$\cos\alpha = \frac{1}{\beta_{SEP}}\left(1 - \frac{1}{\bar{\omega}_r^2}\left(\dot{\theta}^2 \cos^2\phi - \dot{\phi}^2\right)\right)$$

$$\ddot{\theta} = 2\dot{\theta}\dot{\phi}\tan\phi \tag{17}$$

$$\ddot{\phi} = -\dot{\theta}^2 \sin\phi\cos\phi \pm \beta_{SEP}\bar{\omega}_r^2 \sin\alpha$$

Again, feasible spherical orbits are found only if $-1 \leq \cos\alpha \leq 1$, which can be translated into the following constraints on the scaling factor, β_{SEP}, and the in-plane angular velocity, $\dot{\theta}(t)$:

$$\beta_{SEP} \geq 1 - \frac{1}{\bar{\omega}_r^2}\left(\dot{\theta}^2 \cos^2\phi + \dot{\phi}^2\right) \tag{18}$$

$$\dot{\theta}(t) \leq \sqrt{\frac{\bar{\omega}_r^2\left(1 + \beta_{SEP}\right) - \dot{\phi}^2}{\cos^2\phi}} \tag{19}$$

Due to the fact that the in-plane angular velocity is not constant throughout the orbit, the evaluation of the constraints in Eqs. (18) and (19) is less straight forward than for the cylindrical case. Especially Eq. (19) is difficult to evaluate analytically since both the left-hand side and right-hand side of the equation change during the orbit and the location where the difference between the two is minimum needs to be sought for. The evaluation of the constraints will therefore be investigated for each family of spherical NKOs separately, first for oscillating orbits, followed by banded orbits.

Oscillating orbits

For oscillating orbits, it follows from analyses that the maximum value of the right-hand side of Eq. (18) occurs at the initial condition, i.e. at $\phi = \phi_0$. Therefore, the minimum value for the scaling factor is

given by:

$$\beta_{SEP} \geq 1 - \frac{\dot{\theta}_0^2}{\overline{\omega}_r^2} \cos^2 \phi_0 \tag{20}$$

and can be evaluated analytically. Instead, the minimum value of both the left and right-hand sides of Eq. (19) occur upon crossing the (x, y)-plane, i.e. at $\phi = 0$, leading to the following constraint on the in-plane angular velocity:

$$\dot{\theta}_{\phi=0} \leq \sqrt{\overline{\omega}^2 \left(1 + \beta_{SEP}\right) - \dot{\phi}_{\phi=0}^2} \tag{21}$$

Since both $\dot{\theta}_{\phi=0}$ and $\dot{\phi}_{\phi=0}$ cannot be known before integration, the constraint in Eq. (21) can only be determined numerically by integrating the equations of motion and truncating the integration when the constraint is violated. The result, in terms of the feasibility region for the oscillating spherical NKOs is shown in Figure 13 for the same case as used for the cylindrical NKOs: $\rho = 0.9$ and $z_0 = 0.5$ (i.e. $r = 1.03$ and ϕ_0 = 0.16π). Interesting to note is the case where $\beta_{SEP} = 0$ and $\dot{\theta}_0 = 1.095$, which represents the circular Keplerian orbit that lies on the spherical surface.

A first impression of the types of oscillating, cylindrically constrained NKOs that are feasible is provided in Figure 13b) for $\rho = 0.9$ and $z_0 = 0.5$ and for two particular values of the scaling factor. The figures again clearly show the oscillating behavior of these orbits around the (x, y)-plane and hint at the possibility of finding periodic orbits for the spherical case.

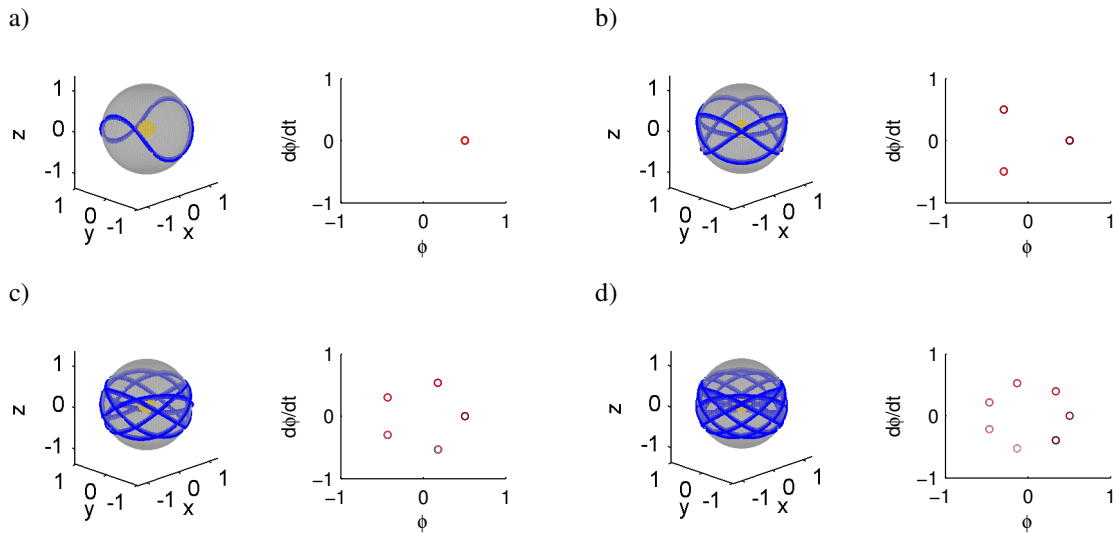a)   b)
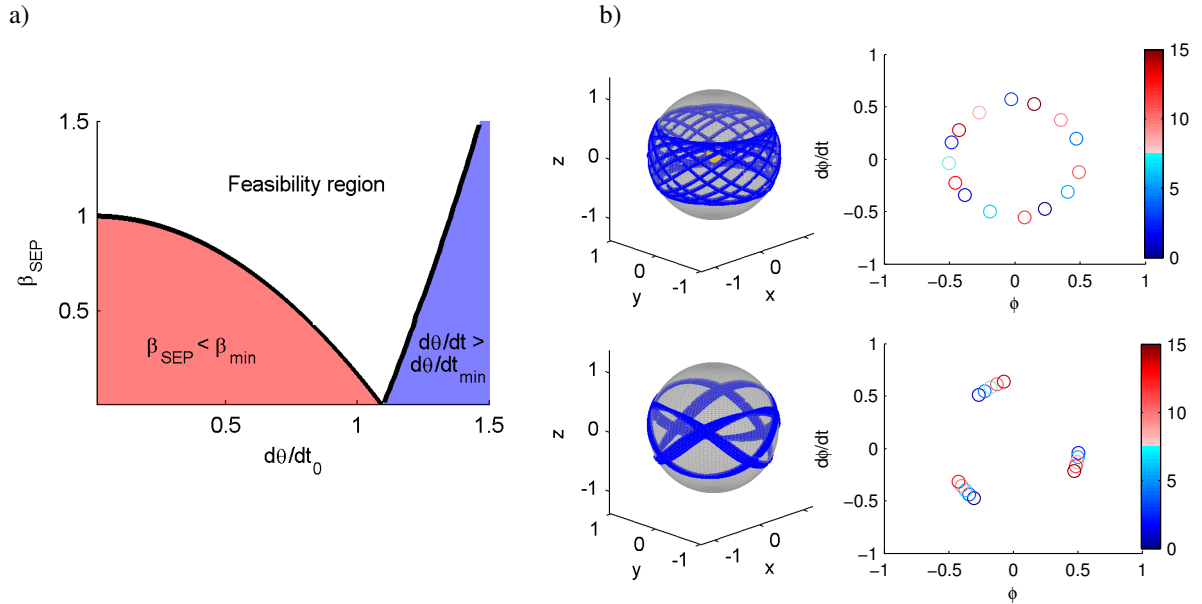
Figure 13 Oscillating, spherical NKOs with inverse-square acceleration law for $\rho = 0.9$ and $z_0 = 0.5$. a) Feasibility region. b) Orbits and Poincaré maps for $d\theta/dt_0 = 1$, $\beta_{SEP} = 0.2$ (top) and $\beta_{SEP} = 0.3$ (bottom).

True periodic orbits are once again sought for using an approach very similar to the one used for oscillating cylindrical orbits. However, while for the cylindrical case the in-plane angular velocity was constant (causing the in-plane angle to be equal to the dimensionless time), this is not the case for the spherical NKOs. Therefore, rather than working with the time, the in-plane angle is monitored: the orbit is integrated forward from its initial conditions until it crosses the (x, y)-plane, which occurs at $\theta = \theta_{\phi=0}$. A full period

of the orbit, P, would thus equal $P = 4\theta_{\phi=0}$, which can be expressed as a fraction of a full revolution as $4\theta_{\phi=0} / 2\pi$ and equals the ratio of in-plane and out-of-plane angular velocities: $\omega_z / \omega = 4\theta_{\phi=0} / 2\pi$. The rest of the approach is equal to the cylindrical case: if this fraction equals an irreducible fraction (e.g. $1/2$, $2/3$, $4/5$, etc.) the orbit is periodic, where the period is given by the nominator of the irreducible fraction. A fine grid search over values for $\dot{\theta}_0$ and β_{SEP} provides the periodic oscillating, spherical orbits with an inverse square acceleration law in Figure 14 with some example periodic orbits in Figure 15.
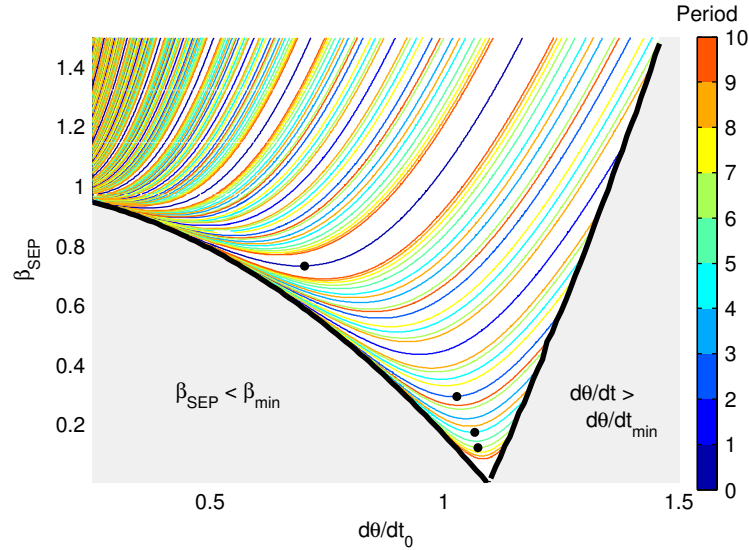
Figure 14 Periodic orbits for oscillating, spherical NKOs with inverse-square acceleration law for $\rho = 0.9$ and $z_0 = 0.5$. The black dots correspond to the orbits in Figure 15.

Figure 15 Orbits (see black dots in Figure 14) and Poincaré maps for oscillating, spherical NKOs with inverse-square acceleration law for $\rho = 0.9$ and $z_0 = 0.5$. a) $d\theta/dt_0 = 0.703$, $\beta_{SEP} = 0.733$. b) $d\theta/dt_0 = 1.027$, $\beta_{SEP} = 0.295$. c) $d\theta/dt_0 = 1.066$, $\beta_{SEP} = 0.175$. d). $d\theta/dt_0 = 1.072$, $\beta_{SEP} = 0.123$.

15

Banded orbits

When considering the plus-sign in the third equation of Eq. (17), banded spherical NKOs can be found. As for the banded cylindrical orbits, the analyses start from the 2D NKOs which are part of the set of spherical NKOs. The required scaling factor to achieve these 2D NKOs, $\beta_{SEP,2D}$, can be found by setting $\dot{\phi} = \ddot{\phi} = 0$ in Eq. (17):

$$\beta_{SEP,2D} = \sqrt{\left(\left(\frac{\omega}{\bar{\omega}_r}\right)^2 \sin\phi\cos\phi\right)^2 + \left(1 - \left(\frac{\omega}{\bar{\omega}_r}\right)^2 \cos^2\phi\right)} \tag{22}$$

Note that, when considering the difference in definition for $\bar{\omega}$ and $\bar{\omega}_r$, Eq. (22) can be shown to equal Eq. (6). Again, by deviating from $\beta_{SEP,2D}$, additional spherically confined orbits can be found: the sub-family of 'north orbits' are created by *increasing* β_{SEP} with respect to $\beta_{SEP,2D}$, while the sub-family of 'south orbits' are created by *decreasing* β_{SEP} with respect to $\beta_{SEP,2D}$. The evaluation of the constraints in Eqs. (18) and (19) is different for each type of orbit, but is very similar to the cylindrical case, as will be discussed below.

To obtain the minimum required value for β_{SEP}, the constraint in Eq. (18) needs to be evaluated at ϕ_{min}, which is known for north orbits ($\phi_{min} = \phi_0$) but unknown for south orbits. The constraint for β_{SEP} can therefore only be determined analytically for north orbits and is evaluated numerically for south orbits:

$$\beta_{SEP,north} \geq 1 - \frac{\dot{\theta}_0^2}{\bar{\omega}_r^2}\cos^2\phi_0 \tag{23}$$

Furthermore, it appears that the constraint on $\dot{\theta}(t)$ can be evaluated at ϕ_{max}, which is known for south orbits $\phi_{max} = \phi_0$, but is unknown for north orbits. For south orbits, the constraint on $\dot{\theta}(t)$ can therefore be determined analytically through:

$$\dot{\theta}_{\phi=\phi_0\ south} = \dot{\theta}_0 \leq \frac{\bar{\omega}_r\sqrt{(1+\beta_{SEP})}}{\cos\phi_0} \tag{24}$$

The resulting feasibility region is shown in Figure 16, which includes the result of the same periodicity analysis as for the oscillating spherical orbits, and as the system's phase space in Figure 17 for the case $\rho = 0.9$ and $z_0 = 0.5$. In Figure 16, the constraint in Eq. (23) is indicated with a thick yellow line (again indicating that 2D NKOs are feasible for all $\dot{\theta}_0$), while the constraint in Eq. (24) is shown with a thick blue line. Although the figure seems to suggest that there is no limit on the allowable value for β_{SEP} for north orbits, such a limit does exist, similarly to the cylindrical case in Figure 7, but only for unrealistically large values for β_{SEP}. Both figures again clearly demonstrate the existence of north and south orbits and by decreasing β_{SEP} far below $\beta_{SEP,2D}$, the phase space once again resembles the phase space of an oscillating orbit.

Considering applications of the Sun-centered spherical NKOs, three distinct uses can be imagined: first, similarly to the cylindrical case, the south orbits that allow a reduction in the required value for β_{SEP} with respect to the 2D NKO and stay close to the 2D NKO can be considered an alternative to the 2D NKO as they require a less demanding propulsion technology. Second, the orbits that cover the poles of the spherical surface, such as the orbits in Figure 18a and Figure 18d, would be very suitable for solar polar observation. Since the poles of the Sun cannot be viewed from conventional orbits that traditionally lie in the ecliptic plane, these NKOs can provide new insights in the interesting physical processes at the poles of the Sun.

Lastly, the orbits that cover a significant part of the spherical surface, such as the oscillating orbits and, for example, the orbit in Figure 18c, would be highly suitable for three-dimensional imaging of the features and structures of the Sun.
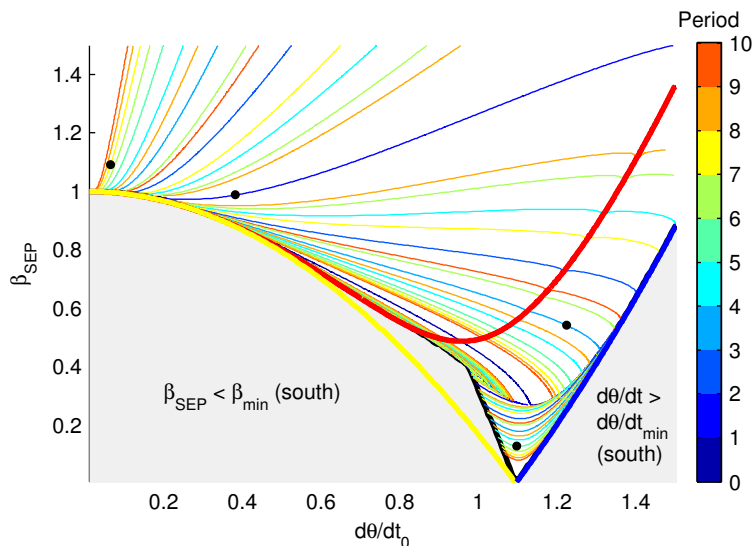
Figure 16 Feasibility region including periodic orbits for banded, spherical NKOs with inverse-square acceleration law for $\rho = 0.9$ and $z_0 = 0.5$. The tick blue line equals Eq. (24), the thick yellow line equals Eq. (23). The black dots correspond to the orbits in Figure 18.
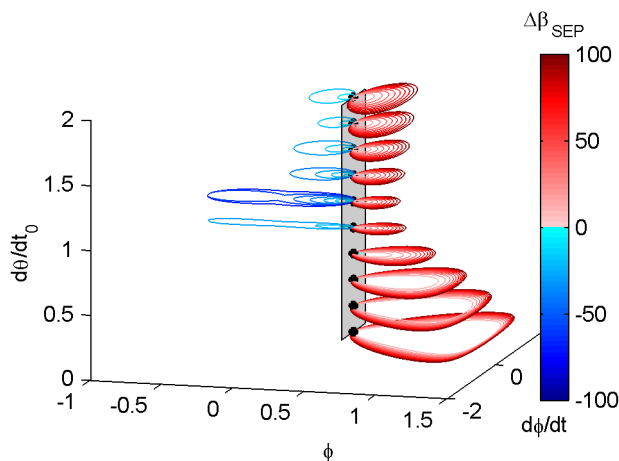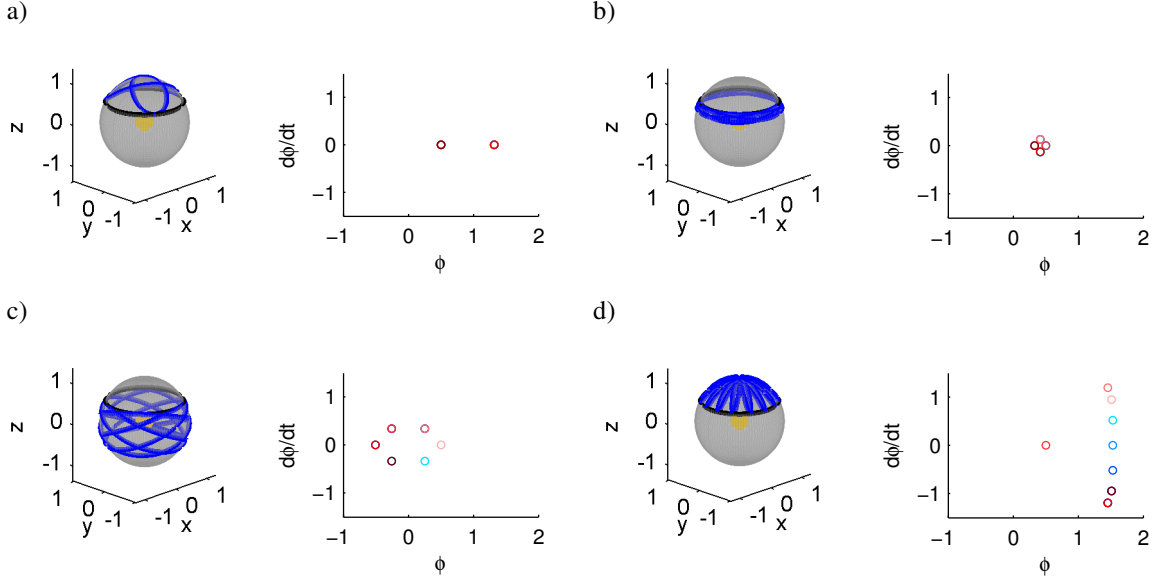

Figure 17 Phase spaces for banded, spherical NKOs with inverse-square acceleration law for $\rho = 0.9$ and $z_0 = 0.5$. Colors indicate percentage deviation from $\beta_{SEP,2D}$ with a step size of 10%.

Solar sail acceleration law

The final case that will be considered includes the banded spherical orbits with a solar sail acceleration law. Using the new definition for $\bar{\omega}_r$, the solar sail acceleration law can now be written as:

$$a = \beta_s \frac{\mu}{r^2} \cos^2 \alpha = \beta_{SEP} \bar{\omega}_r^2 r \cos^2 \alpha \tag{25}$$

which reduces the equations of motion in Eq. (15) to:

Figure 18 Orbits (see black dots in Figure 16) and Poincaré maps for banded, spherical NKOs with inverse-square acceleration law for $\rho = 0.9$ and $z_0 = 0.5$. a) $d\theta/dt_0 = 0.382$, $\beta_{SEP} = 0.987$. b) $d\theta/dt_0 = 1.225$, $\beta_{SEP} = 0.542$. c) $d\theta/dt_0 = 1.097$, $\beta_{SEP} = 0.126$. d). $d\theta/dt_0 = 0.064$, $\beta_{SEP} = 1.091$.

$$\cos\alpha = \sqrt[3]{\frac{1}{\beta_s}\left(1 - \frac{1}{\bar{\omega}_r^2}\left(\dot{\theta}^2\cos^2\phi - \dot{\phi}^2\right)\right)}$$
$$\ddot{\theta} = 2\dot{\theta}\dot{\phi}\tan\phi \tag{26}$$
$$\ddot{\phi} = -\dot{\theta}^2\sin\phi\cos\phi + \beta_s\bar{\omega}_r^2\cos^2\alpha\sin\alpha$$

The feasibility region can once again be derived from the constraint $0 \le \cos\alpha \le 1$, where the lower limit on $\cos\alpha$ once again takes into account the inability of the solar sail to generate an acceleration in the direction of the Sun. This constraint results in a maximum value for the in-plane angular velocity for south orbits that is very similar to the constraint in Eq. (24):

$$\dot{\theta}_{\phi=\phi_0\ south} = \dot{\theta}_0 \le \frac{\bar{\omega}_r}{\cos\phi_0} \tag{27}$$

This constraint equals the maximum allowable in-plane angular velocity for a solar sail 2D NKO, see Eq. (13), but also represents the Keplerian orbit that lies on the spherical surface as mentioned on page 14. Investigating the upper limit on $\cos\alpha$, it appears that for north orbits the same constraint applies as in Eq. (23):

$$\beta_{s,\,north} \ge 1 - \frac{\dot{\theta}_0^2}{\bar{\omega}_r^2}\cos^2\phi_0 \tag{28}$$

The feasibility region in Figure 19 clearly shows these constraints with a yellow and blue line. Note that the constraints on the minimum required lightness number for south orbits and the maximum initial in-plane angular velocity for north orbits can once again only be determined numerically. The latter constraint limits the maximum achievable lightness number for north orbits, although Figure 19 might give the impression that the lightness number can be increased unlimitedly. Furthermore, the red line is the lightness number required for a 2D NKO.

Finally, using the exact same approach as for the other spherical orbits, periodic banded, solar sail spherical orbits can be found, see Figure 19. Some final example periodic orbits are provided in Figure 20.
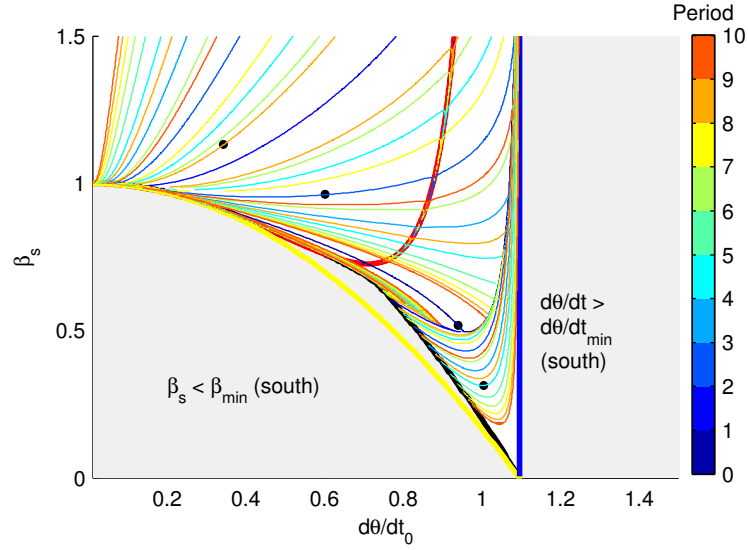
Figure 19 Feasibility region including periodic orbits for banded, spherical NKOs with solar sail acceleration law for $\rho = 0.9$ and $z_0 = 0.5$. The thick blue line equals Eq. (27), the thick yellow line equals Eq. (28). The black dots correspond to the orbits in Figure 20.
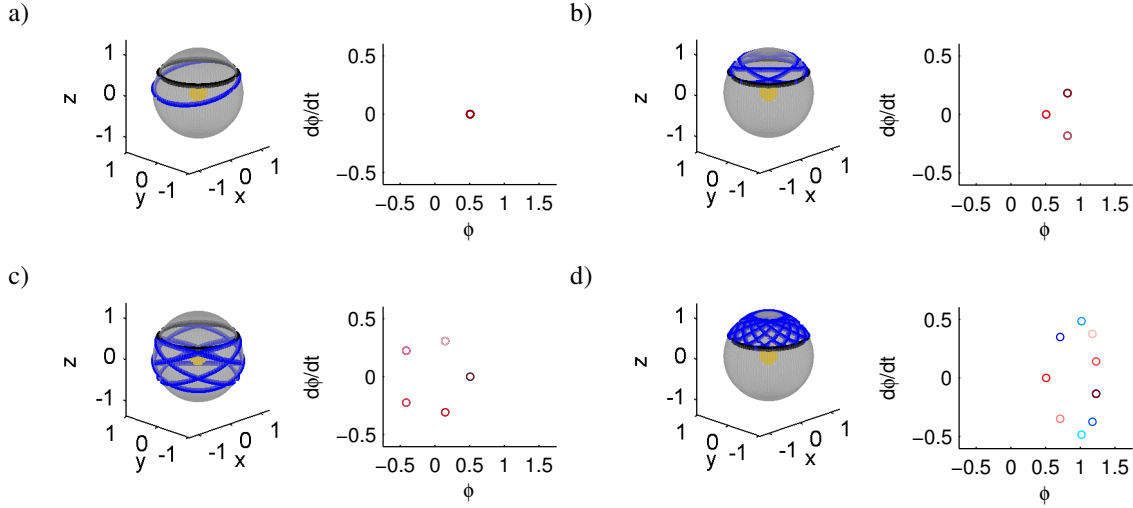
Figure 20 Orbits (see black dots in Figure 19) and Poincaré maps for banded, spherical NKOs with solar sail acceleration law for $\rho = 0.9$ and $z_0 = 0.5$. a) $d\theta/dt_0 = 0.939$, $\beta_s = 0.518$. b) $d\theta/dt_0 = 0.601$, $\beta_s = 0.962$. c) $d\theta/dt_0 = 1.005$, $\beta_s = 0.313$. d). $d\theta/dt_0 = 0.343$, $\beta_s = 1.132$.

CONCLUSIONS

As an extension to the well-known families of two-dimensional (2D) displaced non-Keplerian orbits (NKOs), this paper has introduced three-dimensional Sun-centred NKOs that are constrained to a cylindrical or spherical surface. To maintain these orbits, two types of propulsion have been investigated, including an inverse square acceleration law (mimicking solar electric propulsion) and an ideal solar sail acceleration

law. For both types of orbits and both types of propulsion, the geometrically constrained equations of motion have been derived and by setting further constraints on the in-plane angular velocity and the acceleration magnitude, the set of feasible orbits has been defined. Within this set of feasible orbits, true periodic orbits have been found that can serve a range of space applications: those cylindrical and spherical orbits that allow a reduction in the acceleration magnitude with respect to a 2D NKO but stay close to the 2D NKO from which they bifurcate might provide a viable alternative to the 2D NKO as less demanding propulsion technology is required. Furthermore, spherical orbits that maintain a position high on the spherical surface are considered to be of interest for solar polar observation, while those that cover a significant part of the spherical or cylindrical surface could serve for a 3D mapping of the features and structures of the Sun. A future extension from a Sun-centred case to a planet-centred case will increase the wealth of spacecraft applications that these cylindrically and spherically constrained NKOs can provide even further.

ACKNOWLEDGMENTS

REFERENCES

[1] McInnes, C. R. "Dynamics, Stability, and Control of Displaced Non-Keplerian Orbits," *Journal of Guidance, Control, and Dynamics* Vol. 21, No. 5, 1998, pp. 799-805. Doi: 10.2514/2.4309

[2] McInnes, C. R. "The Existence And Stability Of Families Of Displaced Two-Body Orbits," *Celestial Mechanics and Dynamical Astronomy* Vol. 67, No. 2, 1997, pp. 167-180. Doi: 10.1023/A:1008280609889

[3] McInnes, C., and Simmons, J. F. L. "Solar Sail Halo Orbits. Part I - Heliocentric Case," *Journal of Spacecraft and Rockets* Vol. 29, No. 4, 1992, pp. 466-471. Doi: 10.2514/3.25487

[4] Baig, S., and McInnes, C. R. "Light-Levitated Geostationary Cylindrical Orbits Are Feasible," *Journal of Guidance, Control, and Dynamics* Vol. 33, No. 3, 2010, pp. 782-793. Doi: 10.2514/1.46681

[5] Heiligers, J., Ceriotti, M., McInnes, C. R., and Biggs, J. D. "Displaced Geostationary Orbit Design Using Hybrid Sail Propulsion," *Journal of Guidance, Control, and Dynamics* Vol. 34, No. 6, 2011, pp. 1852-1866. Doi: 10.2514/1.53807

[6] Spilker, T. R. "Saturn Ring Observer," *Acta Astronautica* Vol. 52, 2003, pp. 259-265. Doi: 10.1016/S0094-5765(02)00165-0

[7] Macdonald, M., McInnes, C., Alexander, D., and Sandman, A. "GeoSail: Exploring the Magnetosphere Using a Low-cost Solar Sail," *Acta Astronautica* Vol. 59, 2006, pp. 757-767. Doi: 10.1016/j.actaastro.2005.07.023

[8] Heiligers, J., and McInnes, C. R. "New Families of non-Keplerian Orbits: Solar Sail Motion over Cylinders and Spheres," *3rd International Symposium on Solar Sailing*. Glasgow, United Kingdom, 2013.

[9] Kawaguchi, J. i., Fujiwara, A., and Uesugi, T. "Hayabusa - Its Technology and Science Accomplishment Summary and Hayabusa-2," *Acta Astronautica* Vol. 62, No. 10–11, 2008, pp. 639-647. Doi: 10.1016/j.actaastro.2008.01.028

[10] Russell, C. T., Coradini, A., Christensen, U., De Sanctis, M. C., Feldman, W. C., Jaumann, R., Keller, H. U., Konopliv, A. S., McCord, T. B., McFadden, L. A., McSween, H. Y., Mottola, S., Neukum, G., Pieters, C. M., Prettyman, T. H., Raymond, C. A., Smith, D. E., Sykes, M. V., Williams, B. G., Wise, J., and Zuber, M. T. "Dawn: A Journey in Space and Time," *Planetary and Space Science* Vol. 52, No. 5–6, 2004, pp. 465-489. Doi: 10.1016/j.pss.2003.06.013

[11] Muzi, D., and Allasio, A. "GOCE: The First Core Earth Explorer of ESA's Earth Observation Programme," *Acta Astronautica* Vol. 54, No. 3, 2004, pp. 167-175. Doi: 10.1016/s0094-5765(02)00296-5

[12] Tsuda, Y., Mori, O., Funase, R., Sawada, H., Yamamoto, T., Saiki, T., Endo, T., and Kawaguchi, J. "Flight Status of IKAROS Deep Space Solar Sail Demonstrator," *Acta Astronautica* Vol. 69, No. 9-10, 2011, pp. 833-840. Doi: 10.1016/j.actaastro.2011.06.005

[13] Johnson, L., Whorton, M., Heaton, A., Pinson, R., Laue, G., and Adams, C. "NanoSail-D: A Solar Sail Demonstration Mission," *Acta Astronautica* Vol. 68, 2011, pp. 571-575. Doi: 10.1016/j.actaastro.2010.02.008

[14] L'Garde Inc. "L'Garde - Sunjammer." http://www.lgarde.com/programs/space-propulsion/sunjammer, Accessed 8 May 2013.

[15] McInnes, C. R. *Solar Sailing: Technology, Dynamics and Mission Applications*. Berlin: Springer-Praxis Books in Astronautical Engineering, Springer-Verlag, 1999.

[16] Meserve, B. E. *Fundamental Concepts of Algebra*. New York: Dover Publications, 1982.